

## REPORT DOCUMENTATION PAGE

Form Approved  
OMB No. 0704-0188

Public reporting burden for this collection of information is estimated to average 1 hour per response, including the time for reviewing instructions, searching existing data sources, gathering and maintaining the data needed, and completing and reviewing the collection of information. Send comments regarding this burden estimate or any other aspect of this collection of information, including suggestions for reducing this burden, to Washington Headquarters Services, Directorate for Information Operations and Reports, 1215 Jefferson Davis Highway, Suite 1204, Arlington, VA 22202-4302, and to the Office of Management and Budget, Paperwork Reduction Project (0704-0188), Washington, DC 20503.

1. AGENCY USE ONLY (Leave blank)		2. REPORT DATE March 13, 1996	3. REPORT TYPE AND DATES COVERED Final Report, April 1, 1991 - April 30, 1995	
4. TITLE AND SUBTITLE Dynamics of Electronic and Phonon States in Tunable Solid State Laser Materials			5. FUNDING NUMBERS DAAL03-91-G-0066	
6. AUTHOR(S) P.I. - R. R. Alfano Researchers - V. Petričević, S. G. Demos, D. M. Calistru				
7. PERFORMING ORGANIZATION NAME(S) AND ADDRESS(ES) City College of New York Convent Ave. @ 138 Street New York, NY 10031			8. PERFORMING ORGANIZATION REPORT NUMBER	
9. SPONSORING/MONITORING AGENCY NAME(S) AND ADDRESS(ES) U. S. Army Research Office P. O. Box 12211 Research Triangle Park, NC 27709-2211			10. SPONSORING/MONITORING AGENCY REPORT NUMBER ARO 28426.12-PH-SAT	
11. SUPPLEMENTARY NOTES The view, opinions and/or findings contained in this report are those of the author(s) and should not be construed as an official Department of the Army position, policy, or decision, unless so designated by other documentation.				
12a. DISTRIBUTION/AVAILABILITY STATEMENT  Approved for public release; distribution unlimited			12b. DISTRIBUTION CODE  19960522 082	
13. ABSTRACT (Maximum 200 words)  The objective of this research was to study nonradiative processes occurring in tunable solid state laser crystals, focusing on the first $\text{Cr}^{4+}$ tunable laser crystal, $\text{Cr:M}_2\text{SiO}_4$ developed by our group. Nonradiative processes were investigated in terms of local (ion) - phonon (lattice) mode coupling. A restricted number of phonon modes was shown to be directly involved in the nonradiative deexcitation of $\text{Cr}^{4+}$ . Up-converted-hot-luminescence techniques identify the phonon modes involved in the nonradiative decay, and time resolve Raman scattering allowed for the direct measurement of the dynamics of Raman active phonons involved in the nonradiative relaxation. Resonance Raman scattering identified $\text{Cr}^{4+}$ local modes. This research project has shown that one of the main criteria leading to local-phonon mode coupling which triggers nonradiative processes is energy resonance between local and phonon modes. A minor research effort focused on developing new $\text{Cr}^{4+}$ -doped solid state laser materials. This work has led to growing and characterizing new materials with the potential of lasing in the 1.2 - 1.6 $\mu\text{m}$ near infrared spectral region.				
14. SUBJECT TERMS Nonradiative relaxation, new laser materials, phonon modes, local modes, fluorescence, Raman, $\text{Cr:Mg}_2\text{SiO}_4$ , $\text{Cr:Ca}_2\text{GeO}_4$			15. NUMBER OF PAGES 30	
			16. PRICE CODE	
17. SECURITY CLASSIFICATION OF REPORT UNCLASSIFIED	18. SECURITY CLASSIFICATION UNCLASSIFIED	19. SECURITY CLASSIFICATION OF ABSTRACT UNCLASSIFIED	20. LIMITATION OF ABSTRACT UL	

**Dynamics of Electronic and Phonon States in  
Tunable Solid state Laser Materials**

**FINAL REPORT**

**Principal Investigator : R. R. Alfano**

**Staff : V. Petričević, S. G. Demos , D. M. Calistru**

**Date : March 7, 1996**

**U. S. Army Research Office**

**Contract Number : DAAL03-91-G-0066**

**Institution : City College of New York**

**APPROVED FOR PUBLIC RELEASE;  
DISTRIBUTION UNLIMITED**

## TABLE OF CONTENTS

	pag.
1. Statement of the problem studied.....	1
2. Summary of the most important achievements.....	2
2.1. Time resolved Raman measurements; phonons involved in nonradiative processes.....	2
2.2. Up-converted hot luminescence and electronic bottlenecks...	3
2.3. Resonance Raman and identification of $\text{Cr}^{4+}$ local modes in forsterite.....	4
2.4. Selective phonon modes involved in the nonradiative relaxation.....	6
2.5. Development of new $\text{Cr}^{4+}$ -doped solid-state laser materials....	8
3. Figure Captions.....	12
4. List of Publications.....	14
5. Ph.D. Students graduated during grant period.....	15

## 1. STATEMENT OF THE PROBLEM STUDIED.

The objective of the research project was to study the nonradiative processes occurring in tunable solid state laser crystals.

Following photoexcitation, the impurity ion relaxes radiatively and/or nonradiatively by energy transfer from the hot ion into the lattice. The nonradiative relaxation processes offer an alternate route for the photoexcited ions to dissipate their energy without radiative transition leading to undesirable for the laser action of the active ion loss of quantum efficiency. The understanding of the physics associated with the nonradiative relaxation processes will lead to the selection of the appropriate impurity ion and host crystal to produce lasers of high quantum efficiency and control over the nonradiative relaxation mechanisms.

The time-resolved Raman scattering and the up-converted-hot-luminescence techniques allowed for the identification for the first time of phonon modes involved in nonradiative processes. Resonance Raman scattering identifies in terms of energy and symmetry the lasing ion's local modes, which are the "starting point" for the nonradiative processes. The combined information on the involvement of local and phonon modes in nonradiative processes allows the formulation of general criteria regarding the underlying features which enable local-phonon mode coupling and energy transfer from the ion into the lattice.

The application of the above techniques focused in forsterite ( $\text{Cr}^{4+}:\text{Mg}_2\text{SiO}_4$ ) was carried out in this research. We were able to measure the energy and dynamics of the phonon modes involved in the nonradiative relaxation, the local modes and their symmetry, and electronic bottlenecks associated with the nonradiative relaxation and the electronic states of the excited ions. This research project has lead to the conclusion that the hot ion's local modes couple with (some) phonon (lattice) modes enabling energy dissipation into the lattice. One of the criteria for strong coupling between local and lattice modes is the resonance in energy. Up to this day there is no detailed theory to predict which phonon and local modes are involved in nonradiative processes. Future experimental work in this direction is needed to reveal detailed information on this issue and it will help to obtain the knowledge required for the complete understanding of the nonradiative relaxation processes in tunable solid state laser crystals.

## 2. SUMMARY OF THE MOST IMPORTANT ACHIEVEMENTS

### 2.1. Time resolved Raman measurements; phonons involved in nonradiative processes.

The time dependence of the pump-probe Raman spectrum in chromium-doped forsterite was measured to determine the rise and decay behavior of different Raman-active phonon modes involved in the nonradiative decay.

Cr-doped forsterite was photoexcited above the  $\text{Cr}^{4+}$  lasing level by a train of 450-fs, 590-nm pump pulses and probed by a time-delayed, cross-polarized pulses of same pulse duration and wavelength. An ultrasensitive detector (PIAS-Hamamatsu) was used to monitor the small changes in the relative intensity of anti-Stokes Raman lines due to scattering of both the pump and the probe pulses as a function of pump-probe delay. Different Raman spectra corresponding to the pump and to the probe beam are a consequence of different selection rules for the cross-polarized pump and probe beams. Measuring the ratio of the intensities of the anti-Stokes Raman lines corresponding to the probe beam over the intensity of the Raman lines due to the pump beam for different pump-probe delays, a picture of the dynamics of the nonequilibrium phonons is developed. Applying different polarization of the pump-probe and scattering light with respect to the crystal axis, we investigated most of the Raman active phonon modes of forsterite in the backscattering configuration. We found that the  $225\text{-cm}^{-1}$ ,  $335\text{-cm}^{-1}$  and  $370\text{ cm}^{-1}$  modes exhibit delay time dependent changes of the intensity ratio indicating that these modes are participating in the nonradiative relaxation of forsterite. Fig. 1 displays typical anti-Stokes Raman spectra at two pump-probe time delays. Due to different selection rules for the cross polarized pump and probe beams, different phonon Raman lines were observed for each beam. The  $370\text{ cm}^{-1}$  line is due to the pump beam and therefore, its intensity is independent of delay time ( $t \geq 0$ ). On the other hand, the  $335\text{ cm}^{-1}$  and  $225\text{ cm}^{-1}$  lines arise from the probe beam and are expected to carry the Raman signal from the nonequilibrium phonon population generated by the nonradiative decay following the photoexcitation of the Cr ions by the pump pulse. The salient feature shown in Fig. 1 is the difference in the intensity, denoted by  $\Delta I$ , between the reference  $370\text{ cm}^{-1}$  line and the lines from the probe beam at delays of 1 and 6 ps.

The time dependence of the  $225\text{-cm}^{-1}$ ,  $335\text{-cm}^{-1}$  and  $370\text{ cm}^{-1}$  modes is displayed in Fig. 2. The  $225\text{ cm}^{-1}$  mode profile rises to a maximum nonequilibrium population in  $10 \pm 1.5$  ps and decays with time constant of  $13.8 \pm 3$  ps. The  $335\text{ cm}^{-1}$  mode profile peaks at  $8 \pm 1$  ps and has a decay time of  $10.3 \pm 3$  ps. The maximum

intensity of the  $370\text{ cm}^{-1}$  mode is observed at  $9\pm1.5$  ps and the population decays in  $12.2\pm3.4$  ps. Using a rate equation approach to describe the nonradiative relaxation process we estimated the key relaxation parameters of the system.

## 2.2. Up-converted hot luminescence and electronic bottlenecks.

"Up-converted luminescence" describes the emission from excited state levels populated by excited state absorption (ESA). The up-converted emission is observed at wavelengths lower than the excitation laser wavelength. Up-converted ordinary luminescence (OL) emission arises from transitions between metastable levels and the ground state and the spectral profile depends only on the position of the metastable level. Up-converted hot luminescence (HL) is due to radiative transitions from the manifold of vibronic states populated during the nonradiative decay and occurs immediately after the two-step photoexcitation.

The excitation level ( $E_{EL}$ ) reached after ESA is given by

$$E_{EL}=E_{SL}+h\omega_{\text{photon}}$$

where ( $E_{SL}$ ) is the energy of the storage level (SL). In forsterite, the storage level is the upper lasing level which is the lowest vibronic level of the  ${}^3T_2$  electronic state located at  $9150\text{ cm}^{-1}$ . Ions at the SL absorb a photon to reach an excitation level at energy given by the sum of the energies of the SL and the photon absorbed. Up-converted HL for different laser wavelengths is shown in Fig. 3. The lower profile was obtained under 617 nm (2.01 eV) laser excitation to reach an excitation level at 3.145 eV (2.01+1.135 eV). Pumping with 650 and 690 nm laser light the second and third spectral profiles were obtained. The energy of the excitation levels are at 3.043 eV and 2.932 eV, respectively. Up-converted HL for 740 nm excitation to reach the 2.811 eV level is shown in the upper profile of Fig. 3. In all cases, three main peaks appear with the highest energy peak positioned at exactly the two-step excitation energy. These peaks reveal the phonon modes involved in the vibronic relaxation. The energy of the phonons is given by the difference in energy between successive peaks in the HL emission. The measured energy of these modes is  $513\pm12\text{ cm}^{-1}$  and  $325\pm12\text{ cm}^{-1}$ .

Using 1064 nm excitation, the excited ions will reach 2.3 eV within the excited state absorption (ESA) process. Up-converted HL under 1064 nm excitation is shown in Fig. 4. A number of peaks are present with the highest energy peak at 2.3 eV. These peaks indicate the phonon modes involved in the nonradiative relaxation in this part of the excited state which are  $323\pm15\text{ cm}^{-1}$  and  $218\pm15\text{ cm}^{-1}$ .

Fig. 5 shows the overall upconverted HL emission profile obtained under 710 nm excitation. Two bands of stronger emission located at  $2.43 \pm .15$  eV (sector B) and  $2.05 \pm .12$  eV (sector C) indicate the presence of electronic bottlenecks. The electronic bottleneck at 2.05 eV is also shown in Fig. 4 under 1064 nm excitation. The nonradiative relaxation slows down in these parts of the excited state resulting to a stronger HL emission. The slowdown of the nonradiative relaxation arises from the energy level structure of the excited ions and electron-phonon coupling.

Up-converted luminescence under 532 nm excitation is shown in Fig. 6. Two regions A and B are noted. The first from a series of peaks appears at  $27945 \text{ cm}^{-1}$  in section A and they are consistent with up-converted HL. At lower energies a much stronger emission is observed (section B). The lifetime of this emission (B) was measured with a streak camera to be 395 ps. The Tanabe-Sugano energy diagram of  $\text{Cr}^{4+}$ -doped forsterite suggests that this emission originates from the  ${}^3\text{T}_1(\text{t}_2\text{e})$  electronic state. The narrow peak at  $26,450 \text{ cm}^{-1}$ , corresponding to the zero-phonon transition, provides the exact position of this electronic state with respect to the ground state ( ${}^3\text{A}_2$ ). The integrated intensity of  ${}^3\text{T}_1(\text{t}_2\text{e}) \rightarrow {}^3\text{A}_2$  emission (B) is estimated to be  $\approx 600$  times stronger than the emission from the highest energy vibronic level (first narrow peak in up-converted HL emission in A). Therefore, the lifetime of the highest energy vibronic level is estimated to be  $\approx 660$  femtoseconds providing an estimation of the nonradiative relaxation rate in this part of the excited state.

The above results reveal the dynamics of phonon modes involved in the nonradiative relaxation of  $\text{Cr}^{4+}$  ions in forsterite. The up-converted HL technique was used to study the nonradiative relaxation and electron-phonon coupling in  $\text{Ni}^{2+}:\text{MgO}$ . We found that the phonon mode involved in the nonradiative relaxation of the Ni ions in the MgO host crystal is  $395 \pm 15 \text{ cm}^{-1}$ . In addition, applying this technique on  $\text{Cr}^{4+}:\text{Mg}_2\text{GeO}_4$  the preliminary result show that the phonons involved in the nonradiative relaxation of this forsterite analog crystal are  $450 \pm 15$ ,  $330 \pm 15$  and  $240 \pm 15 \text{ cm}^{-1}$ .

### 2.3. Resonance Raman and identification of $\text{Cr}^{4+}$ local modes in forsterite.

The resonance Raman scattering technique allows the identification in terms of energy and symmetry of the lasing ion's local modes. When the crystal is excited with a wavelength matching one of the ion's absorption bands, additional peaks appear in the Raman spectrum due to a selective enhancement described by the A

and B terms of Albrecht's theory. The  $\text{Cr}^{4+}:\text{Mg}_2\text{SiO}_4$  sample was excited with 575 nm,  $E_i // a$  in the crystal's  $Pbnm$  notation, which corresponds to the  ${}^3A_2 \rightarrow {}^3B_2({}^3T_1)$   $\text{Cr}^{4+}$  dipole allowed transition. The  $\text{Cr}^{4+}$  ion is positioned in a tetrahedral distorted symmetry. In the  $T_d$  molecular symmetry, in first neighbor interaction approximation, the  $\text{Cr}^{4+}$  ion has nine normal modes of vibration distributed among the irreducible representations of  $T_d$  in the following manner :

$$\Gamma_{T_d} = A_1 + E + 2T_2$$

If orthorhombic distortions are taken into account, the degeneracy of the 4 representations describing the internal vibrations of the  $\text{Cr}^{4+}\text{O}_4$  molecule is completely lifted giving rise to  $6A'$  and  $3A''$  local modes. 7 local modes were identified at room temperature measurements for  $\text{Cr}^{4+}:\text{Mg}_2\text{SiO}_4$  as follows : 5  $A'$  modes at 253, 290, 498, 690 and  $764\text{ cm}^{-1}$  and 2  $A''$  modes at 480 and  $740\text{ cm}^{-1}$ . These modes are shown in Fig. 7. In the first neighbor interaction approximation, without taking into account the orthorhombic distortions it was estimated that the  $\text{CrO}_4$  molecule is looser bound than the  $\text{SiO}_4$  molecule, the  $\text{Cr}^{4+}\text{-O}$  force constant decreasing by  $\approx 13 - 29\%$  (model dependent) if compared to the  $\text{Si-O}$  force constant. The following set of equations was derived for computing the force constants for the  $\text{Cr}^{4+}\text{O}_4$  molecule internal vibrations described by  $\Gamma_{T_d}$  :

$$\begin{aligned}\omega_{A_1}^2 &= \frac{k_1 + 4k_2}{m} \\ \omega_E^2 &= \frac{4k_2}{m} \\ \omega_{T_2}^2 &= \frac{k_1}{m} \left(1 + \frac{4m}{3M}\right) + \frac{4k_2}{3m \left(1 + \frac{4m}{3M}\right)} \\ \omega_{T_2}^2 &= \frac{\frac{2k_2}{3} + 2k_1 \left(\frac{4m}{3M}\right)}{m \left(1 + \frac{8m}{3M}\right)}\end{aligned}$$

where  $\omega_i$  are the frequencies of the 4  $T_d$  normal modes,  $m$  the O mass,  $M$  the Cr mass,  $k_1$  the  $\text{Cr}^{4+}\text{-O}$  force constant and  $k_2$  the O-O force constant. The first two equations together with the mean measured values  $\omega_1 = 765\text{ cm}^{-1}$  and  $\omega_2 = 489\text{ cm}^{-1}$  allow the estimation of  $k_1 = 3.27\text{ mdyne/\AA}$  and  $k_2 = 0.57\text{ mdyne/\AA}$  for the  $\text{Cr}^{4+}\text{-O}$  molecule, to be compared to  $k_1 = 3.75\text{ mdyne/\AA}$  and  $k_2 = 0.716\text{ mdyne/\AA}$  for the  $\text{Si}^{4+}\text{-O}$  molecule. The remaining two equations allow to verify the correctness of the mode assignment. The computed values for the 2  $T_2$  modes at  $737$  and  $293\text{ cm}^{-1}$  are



in good agreement with the mean measured values at 715 and 272  $\text{cm}^{-1}$ , respectively, verifying the mode assignment.

#### 2.4. Selective phonon modes involved in the nonradiative relaxation.

The vibrational state of an excited impurity ion immediately after photoexcitation can be described as a linear combination of electronic and vibrational states associated with the excited ion. The nonradiative relaxation involves the transfer of energy from the ion into the lattice via the generation of phonons. The link between the impurity ion and the lattice environment are the impurity ion modes (local modes) which can efficiently couple to phonon modes and transfer their energy into the lattice modes. It is likely that phonon modes participating in the nonradiative relaxation are those that ensure some resonance with the local modes. Resonance occurs when a) the local modes have similar energies with phonon modes (the density of states of the phonon spectrum is high at the energy of the local mode) and the energy is transferred directly from the ion mode into the lattice mode and b) the sum of the energies of two (or more) phonon modes is close to the energy of a local mode and in that case, the energy is transferred via the generation of two (or more) phonon modes from the breakdown of the local mode. The first type of resonance is a first order phonon process, while the second type involves the emission of at least two phonons and is a second (or higher) order phonon process. If resonance of the first type exists between the ion and the lattice modes it will dominate the nonradiative process, providing the tunnel for energy transfer from the ion into the lattice by local-phonon mode coupling.

Fig. 8 schematically depicts possible first order processes taking place during the energy transfer from the ion into the lattice, which depend both on local-phonon mode energy resonance and coupling strength. The excess energy of the ion is transferred into the lattice through local-phonon mode coupling. Local modes with frequencies very close to phonon modes (energy resonance) can couple with them (band vibrations) and serve as the channel for energy transfer from the excited ion into the lattice. Local modes which are in resonance with phonon modes but are weakly coupled to them (pseudolocalized vibrations) can not transfer energy efficiently into the lattice and lead to weak nonradiative processes. Finally, local modes having very different frequency than phonon modes (localized vibrations) will not participate, in first order processes, in the nonradiative relaxation because they are off-resonance with the lattice modes.

The  $\text{Cr}^{4+}$  local modes which, according to the previous discussion, are the starting point for nonradiative processes, have been measured using resonance Raman scattering at : 253, 288, 346, 361, 390, 408, 420, 468, 477, 499, 526, 691, 742, 765 and  $820\text{ cm}^{-1}$ . The energy resonance between local modes and those phonon modes which participate in nonradiative processes is shown in Fig. 9. The phonons which are active in nonradiative processes are positioned at 225, 335 and  $370\text{ cm}^{-1}$  and are shown with thin line. The thick-line profile shows the resonance Raman spectrum obtained under 572 nm excitation, in c(aa)b geometry and contains  $A_g$  phonons. The intensity of the resonance Raman spectrum was reduced  $\sim 2$  times if compared to the phonon spectrum (thin line). Five  $\text{Cr}^{4+}$  local modes marked by an asterisk (\*) appear in addition to the phonon modes. The local modes are positioned at 253, 288, 346, 361 and  $390\text{ cm}^{-1}$ . Sector A in fig. 9 indicates the spectral width of the  $253\text{ cm}^{-1}$  local mode showing the overlap with the  $225\text{ cm}^{-1}$  phonon mode. Sector B in fig. 9 shows the spectral width of the 346, 361 and  $390\text{ cm}^{-1}$  local modes which are overlapping with the 335 and  $370\text{ cm}^{-1}$  phonon modes ensuring resonance in energy. The resonance explains the selective energy transfer from the local modes to phonon modes.

The temporal and spectral results obtained in forsterite provide a direction to assemble a general criterion regarding the participating phonon modes in nonradiative relaxation of impurity ions in dielectric crystals. The phonon spectrum of the host crystal should be compared with the local mode spectrum to determine if there are any band vibrations in resonance with phonon modes that can efficiently couple the impurity ion with the lattice. If such resonance exists, strong nonradiative relaxation may be expected.

Understanding of the physics involved in the nonradiative relaxation will help design better lasers and to "control or alter" the relaxation processes by using coherent driven vibronic - electronic effects. It is known that the same transition metal ion implanted in different host crystals can result in a crystal that may exhibit no emission at all or it may be an excellent laser crystal. The wide variety of resulting quantum efficiencies depends on the ion-lattice coupling strength which allows the photoexcited ions to relax to the ground state nonradiatively. If we know the details of the ion-lattice system we will be able to choose the impurity ion and the host crystal in order to produce crystals that have the desired properties such as mismatch between the localized and lattice modes.

## 2.5. Development and Spectroscopy of New $\text{Cr}^{4+}$ -Doped Materials

The demonstration of laser operation of chromium-doped forsterite ( $\text{Cr:Mg}_2\text{SiO}_4$ ) and subsequent identification of tetravalent chromium ( $\text{Cr}^{4+}$ ) residing in tetrahedral environment as the lasing ion, have generated growing interest in this material, as well as other crystals that may accommodate  $\text{Cr}^{4+}$  in their structure. During the reporting period, in conjunction with a co-sponsored by NSF grant to grow crystal for lasers, a number of  $\text{Cr}^{4+}$ -based crystals were grown and investigated their basic spectroscopic properties for potential laser applications. Problems associated with the development of these novel laser materials include very weak or nonexistent luminescence due to strong nonradiative relaxation and, in the case of materials with strong emission, growth difficulties.

In our research efforts to develop new  $\text{Cr}^{4+}$ -doped solid-state laser materials we have concentrated our work on host crystals of olivine structure which is analog to forsterite. We have focused on crystals of olivine structure primarily because these crystals are isostructural with forsterite and are among the few materials that exhibit strong  $\text{Cr}^{4+}$  luminescence. It is believed that in crystals with olivine structure such as forsterite, extremely distorted tetrahedron occupied by the  $\text{Cr}^{4+}$  ion provides a low-symmetry crystal field that may relax the electric dipole transition selection rules resulting in high quantum efficiencies. The olivine structure type belongs to the orthorhombic space group:  $\text{Pbnm}$ . It has a tetrahedral site  $\text{Td}(\text{C}_s)$  and two distinct octahedrally coordinated sites, M1 with inversion ( $\text{C}_i$ ) and M2 with mirror ( $\text{C}_s$ ) point symmetry. In forsterite, ( $\text{Mg}_2\text{SiO}_4$ )  $\text{Mg}^{2+}$  ions occupy two octahedral sites while  $\text{Si}^{4+}$  is tetrahedrally coordinated. Unfortunately, both the  $\text{Cr}^{3+}$  and  $\text{Cr}^{2+}$  ions are a good match in size with  $\text{Mg}^{2+}$ . The stabilization of  $\text{Cr}^{2+}$  is particularly undesirable since it may cause weak absorption in the lasing wavelength region. For that reason different olivines were considered as potential hosts in order to eliminate formation of those two ionic states.  $\text{Cr}^{3+}$  and  $\text{Cr}^{2+}$  are incompatible with  $\text{Ca}^{2+}$  due to large size mismatch. We have attempted growth of a group of silicate olivine crystals, such as  $\text{CaMgSiO}_4$  (Monticellite),  $\text{Ca}_2\text{SiO}_4$  (CAS),  $\text{Sr}_2\text{SiO}_4$  (SAS) and  $\text{Ba}_2\text{SiO}_4$  (BAS), primarily because of the similarity of their crystal structure to the structure of forsterite and the large size mismatch between the sixfold coordinated  $\text{Ca}^{2+}$ ,  $\text{Sr}^{2+}$ , and  $\text{Ba}^{2+}$  and the unwanted  $\text{Cr}^{3+}$  and  $\text{Cr}^{2+}$ . The preliminary measurements of the absorption spectra of  $\text{Cr:CaMgSiO}_4$  have shown features that are strikingly similar to those observed in the absorption spectra of  $\text{Cr:Mg}_2\text{SiO}_4$ , the only difference being a slight red shift.

The emission spectra of Cr: CaMgSiO<sub>4</sub> and Cr: Ca<sub>2</sub>SiO<sub>4</sub> were measured for 670-nm excitation at room temperature and at liquid nitrogen temperature. The spectra are shown in Fig. 10. Both results were compared with the emission of a laser-quality Cr: Mg<sub>2</sub>SiO<sub>4</sub> crystal for the same level of excitation. The room-temperature emission spectra of Cr: Mg<sub>2</sub>SiO<sub>4</sub> and Cr: CaMgSiO<sub>4</sub> consist of two broad emission bands, one in the 700 - 1000 nm region, attributed to the Cr<sup>3+</sup> ion, and a band due to Cr<sup>4+</sup> spanning the 1000 - 1500 nm range. The peak of the Cr: CaMgSiO<sub>4</sub> emission is shifted ~ 50 nm into the infrared with respect to the peak of the Cr: Mg<sub>2</sub>SiO<sub>4</sub>. The room-temperature emission spectrum of Cr: Ca<sub>2</sub>SiO<sub>4</sub> shows only one band attributed to Cr<sup>4+</sup>, indicating that in the crystal structure of Ca<sub>2</sub>SiO<sub>4</sub> only the Cr<sup>4+</sup> substitution takes place. In small (<1mm) crystals that we were able to grow, the only ionic state that was stabilized is the tetrahedral Cr<sup>4+</sup> which exhibits strong emission and relatively long room-temperature fluorescence lifetime of ~15 ms. The peak of the emission band is shifted over 100 nm farther into the infrared region as compared to the peak of Cr: Mg<sub>2</sub>SiO<sub>4</sub>. The low temperature emission spectrum of Cr: Ca<sub>2</sub>SiO<sub>4</sub> is characterized by a sharp zero-phonon line followed by a vibrational sideband very similar to the low-temperature spectrum of Cr: forsterite. The zero-phonon line has been shifted ~ 110 nm towards the infrared when compared to Cr: Mg<sub>2</sub>SiO<sub>4</sub>, due to the larger size of the SiO<sub>4</sub> tetrahedron and consequently lower crystal field at the Si site. The low temperature emission spectrum of Cr: CaMgSiO<sub>4</sub> did not reveal any sharp line structure, with only a hint of a zero-phonon line appearing at ~ 1125 nm. It is important to note that although of inferior optical quality, emission of Cr: Ca<sub>2</sub>SiO<sub>4</sub> is almost an order of magnitude stronger than that of Cr: Mg<sub>2</sub>SiO<sub>4</sub>, and Cr: CaMgSiO<sub>4</sub> displays emission at least as strong as that of Cr: forsterite for similar pump powers. Chromium-doped Sr<sub>2</sub>SiO<sub>4</sub> and Ba<sub>2</sub>SiO<sub>4</sub> exhibit very quenched fluorescence.

Unfortunately, monticellite does not melt congruently so that large crystals can not be grown directly from the melt. Large crystals of Ca<sub>2</sub>SiO<sub>4</sub> are impossible to grow because during the growth and cooling process this material undergoes a sequence of phase transitions, the last one that converts the crystal into g (olivine) phase occurring at a temperature lower than 500°C which prevents growth of crystals larger than 1 mm. For that reason, we tried to grow its germanium analog, which does not exhibit any similar phase transitions below 1450°C. For that reason we have considered germanates of olivine structure. Germanate olivines looked particularly promising since there is better size match of the ionic radii of Cr<sup>4+</sup> and Ge<sup>4+</sup>, and larger infrared shift is expected due to larger size of the Ge tetrahedra, and

consequently lower crystal field at the Ge site. Also, they are congruently melting and do not undergo any catastrophic phase transitions. However, germanates are hard to grow using standard growth techniques such as Czochralski pulling due to high volatility of  $\text{GeO}_2$  at temperatures above  $1450^\circ\text{C}$ . Cr-doped olivines, materials that show most promise for laser operation, melt at temperatures well above  $1800^\circ\text{C}$ , making growth of germanate olivines practically impossible using the standard Czochralski method. Therefore, it is imperative to use low-temperature methods for the synthesis of these promising laser materials or to investigate stability of solid solutions with chemical formula  $\text{Cr:Mg}_{2-x}\text{Ca}_x\text{Si}_{1-y}\text{Ge}_y\text{O}_4$ , ( $x=1-2$ ;  $0.45 < y < 1$ ).

$\text{Ca}_2\text{GeO}_4$  exists in two modifications with the phase transition occurring at  $1453^\circ\text{C}$ . The low-temperature phase is isostructural with forsterite and has olivine-type structure with space group Pbm $\bar{n}$ . The lattice parameters of  $\text{Ca}_2\text{GeO}_4$  are:  $a=5.240 \text{ \AA}$ ,  $b=11.400 \text{ \AA}$ , and  $c=6.790 \text{ \AA}$ . Since  $\text{Cr}^{4+}$  and  $\text{Ge}^{4+}$  have the same valence and very similar ionic radii ( $0.41 \text{ \AA}$  vs.  $0.39 \text{ \AA}$ ) the  $\text{Cr}^{4+}$  incorporation into the germanium tetrahedral site of  $\text{Ca}_2\text{GeO}_4$  is ideal. At the same time octahedral  $\text{Ca}^{2+}$  is much larger ion ( $1 \text{ \AA}$ ) than either  $\text{Cr}^{3+}$  ( $0.615 \text{ \AA}$ ) or  $\text{Cr}^{2+}$  ( $0.73 \text{ \AA}$ ).

The absorption spectra of  $\text{Cr:Ca}_2\text{GeO}_4$  for three different crystal orientations, presented in Figure 11, show features that are strikingly similar to those observed in the absorption spectra of chromium-doped forsterite and other olivines, the only difference being significant red shift. We attribute the absorption bands observed in the spectra exclusively to the transitions of the  $\text{Cr}^{4+}$  ion.

The emission spectra of  $\text{Cr:Ca}_2\text{GeO}_4$  were measured for 670-nm excitation at room temperature and at liquid nitrogen temperature. Both results were compared with the emission of a laser-quality  $\text{Cr:forsterite}$  and  $\text{Cr:Mg}_2\text{GeO}_4$  crystal for same level of excitation. The measured spectra are shown in Figure 12. The upper two spectra consist of two broad emission bands, one in the 700-1000 nm region, attributed to the  $\text{Cr}^{3+}$  ion, and a band due to  $\text{Cr}^{4+}$  spanning the 1000-1500-nm range. The room-temperature emission spectrum of  $\text{Cr:Ca}_2\text{GeO}_4$  shows only one band with a maximum at 1290 nm which is attributed to  $\text{Cr}^{4+}$ , indicating that in the crystal structure of  $\text{Ca}_2\text{GeO}_4$  only the  $\text{Cr}^{4+}$  substitution takes place. The absence of  $\text{Cr}^{3+}$  band indicates a more efficient  $\text{Cr}^{4+}$  laser material. The zero-phonon peak of the emission band is shifted  $\sim 110 \text{ nm}$  farther into the infrared region as compared to the peak in forsterite. The low temperature emission spectrum of  $\text{Cr:Ca}_2\text{GeO}_4$  is characterized by a sharp zero-phonon line at 1200 nm followed by a vibrational sideband very similar to the low-temperature spectrum of  $\text{Cr:forsterite}$ . The zero-

phonon line has been shifted over  $\sim 110$  nm towards the infrared when compared to Cr: Mg<sub>2</sub>SiO<sub>4</sub>, due to the larger size of the GeO<sub>4</sub> tetrahedron and consequently lower crystal field at the Ge site.

Fluorescence lifetime of Cr<sup>4+</sup> in Ca<sub>2</sub>GeO<sub>4</sub> for 1064-nm excitation has been measured to be 15 ms. The room temperature fluorescence lifetime of Cr:Ca<sub>2</sub>GeO<sub>4</sub> is five times longer than that of Cr:forsterite, which could result in room temperature laser operation that is less affected by nonradiative processes. At 8 K, the fluorescence lifetime is 25 ms, indicating again that nonradiative processes is not the dominant relaxation mechanism in Cr<sup>4+</sup>:Ca<sub>2</sub>GeO<sub>4</sub>.

In conclusion, this spectroscopic investigation demonstrates the suitability of the Cr<sup>4+</sup>-doped crystals for laser applications. Based on these preliminary spectroscopic measurements, we conclude that Cr:Ca<sub>2</sub>GeO<sub>4</sub> represents a potential candidate for new tunable solid-state laser material based on the Cr<sup>4+</sup> ion with the tuning range covering the 1.3 - 1.6  $\mu$ m near infrared spectral region.

### 3. Figure captions.

**Figure 1:** Anti-Stokes Raman spectra for  $\Delta\tau=1$  ps (thick line) and  $\Delta\tau=6$  ps (thin line) delay times. Each spectrum contains Raman lines arising from the pump and the probe beams.  $\Delta I$  denotes the increase in intensity of the 225 and 335  $\text{cm}^{-1}$  Raman lines of the probe beam at  $\Delta\tau=6$  ps. The scattering configuration is  $P_{\text{pump}}//c$ ,  $P_{\text{probe}}//b$  and  $P_{\text{scatt.}}//b$ -axis of the crystal.

**Figure 2:** Temporal behavior of the intensity of a) the 225  $\text{cm}^{-1}$ , b) 335  $\text{cm}^{-1}$ , and c) 370  $\text{cm}^{-1}$  phonon modes as a function of pump-probe delay time. The thick line represents the best fit when an initially populated intermediate state (bottleneck) is taken into account. The thin line is the best fit without the assumption of the intermediate state.

**Figure 3:** Up converted hot luminescence spectra following excited state absorption under: 617 nm excitation (lower profile), 650 nm excitation, 690 nm excitation and 740 nm excitation (upper profile) at liquid nitrogen temperature.

**Figure 4:** Up-converted hot luminescence under 1064 nm excitation. The laser polarization ( $P_e$ ) is parallel to b axis and the emission polarization ( $P_s$ ) is a)  $P_s//b$  and b)  $P_s//c$  axis of the crystal at backscattering geometry. The sample was at liquid nitrogen temperature.

**Figure 5:** Up-converted HL under 710 nm laser excitation. The dynamics of the process is depicted in the insert at the right. The size of the bars in the vibrational relaxation indicates slowing through bottleneck. Sector A is the part of the emission occupied by the phonon steps while sectors B and C represent the two electronic bottlenecks.

**Figure 6:** Up-converted luminescence under 532 nm excitation. Sector A is due to up-converted hot luminescence. Sector B is due to ordinary luminescence from the  $^3T_1(t_2e)$  electronic state. The sample was held at liquid nitrogen temperature.

Figure 7: Resonant Raman spectra in the  $A_g$ ,  $B_{2g}$  and  $B_{3g}$  symmetry configurations. The sample was held at liquid nitrogen temperature. The 15 local modes observed in the first order Stokes spectrum are denoted with asterisk.

Figure 8: Schematic depicting the impurity ion and host lattice modes. The energy of the photoexcited impurity ion is transferred into the phonon modes that are in resonance with the local modes of the ion.

Figure 9: Raman (thin line) and resonance Raman (thick line) spectra of  $\text{Cr:Mg}_2\text{SiO}_4$ .  $\text{Cr}^{4+}$  local modes appear in addition to phonon modes and are marked with an asterisk (\*). Overlap between local modes(\*) and phonon modes (thin line) shows resonance in energy between local and phonon modes.

Figure 10. Fluorescence spectra of forsterite ( $\text{Cr:Mg}_2\text{SiO}_4$ ), monticellite ( $\text{Cr:CaMgSiO}_4$ ), and  $\text{Cr:Ca}_2\text{SiO}_4$  for 670-nm excitation, at room temperature (thicker line) and at liquid nitrogen temperature (thin line).

Figure 11. Polarized absorption spectra of  $\text{Cr:Ca}_2\text{GeO}_4$  for three different crystal orientations.

Figure 12. Fluorescence spectra of Forsterite ( $\text{Cr:Mg}_2\text{SiO}_4$ ),  $\text{Cr:Mg}_2\text{GeO}_4$  and  $\text{Cr:Ca}_2\text{GeO}_4$  for 670-nm excitation, at room temperature (thicker line) and at liquid nitrogen temperature (thin line). Note the absence of  $\text{Cr}^{3+}$  emission bands in the spectra of  $\text{Cr:Ca}_2\text{GeO}_4$ .



#### 4. LIST OF PUBLICATIONS

1. S. G. Demos, J. M. Buchert and R. R. Alfano, "Time Resolved Nonequilibrium Phonon Dynamics in the Nonradiative Decay of Photoexcited Forsterite" *Appl. Phys. Lett.* 61 (6) 660 (1992).
2. S. G. Demos, and R. R. Alfano, "Upconverted Luminescence from Nonequilibrium Vibronic States of Cr Ions in Forsterite", *Phys. Rev. B*, 46, 8811, (1992).
3. S. G. Demos, Y. Takiguchi, and R.R. Alfano, "Upconverted Hot Luminescence Spectroscopy Investigation of Nonradiative Relaxation in Forsterite", *Optics Lett.*, 18, 522 (1993).
4. Li Yang, V. Petričević, and R. R. Alfano, "Advances in Cr<sup>4+</sup>-Doped Tunable Solid-State Lasers", *Novel Laser Sources and Applications*, J. F. Becker, A. C. Tam, J. B. Gruber, and L. Lam, Editors, Proceedings of a workshop held November 12-13, 1993, San Jose, California, SPIE Optical Engineering Press, pp. 103-115 (1994).
5. D. M. Calistru, W. B. Wang, V. Petričević, and R. R. Alfano, "Resonance Raman Scattering in Cr<sup>4+</sup>-Doped Forsterite", *Phys. Rev. B* 51, 14980 (1995).
6. S. G. Demos, V. Petričević, and R. R. Alfano, "Up-converted Luminescence and Excited-State Excitation Spectroscopy of Cr<sup>4+</sup> Ions in Forsterite", *Phys. Rev. B*, 52, 1544, (1995).
7. S. G. Demos and R.R. Alfano, "Subpicosecond Time Resolved Raman Investigation of Optical Phonon Modes in Cr-doped Forsterite", *Phys. Rev. B*, 52, 987, (1995).
8. S. G. Demos, B. Y. Han and R. R. Alfano, "Phonon Mode and Electronic Bottleneck Associated With the Nonradiative Relaxation in Ni<sup>2+</sup> doped MgO", *Appl. Phys. Lett.* 67 (5) 635 (1995).
9. A. Seas, V. Petričević, and R. R. Alfano, "Generation of Sub-100-fs Pulses From a Continuous-Wave Mode-Locked Chromium-Doped Forsterite Laser", *Opt. Lett.* 17, 937 (1992).
10. A. Seas, V. Petričević, and R. R. Alfano, "60-fs Chromium-Doped Forsterite Laser", *Ultrafast Phenomena VIII*, Proceedings of the 8th International Conference, J. L Martin, A. Migus, G. A. Mourou, A. H. Zewail, eds. , Springer (1993).
11. A. Seas, V. Petričević, and R. R. Alfano, "Self Mode-Locked Chromium-Doped Forsterite Laser Generates 50-fs Pulses", *Opt. Lett.* 18, 891 (1993).

**5. Ph.D. Students Graduated During Grant period.**

1. Stavros Demos (1993)
2. Antonios Seas (1993)

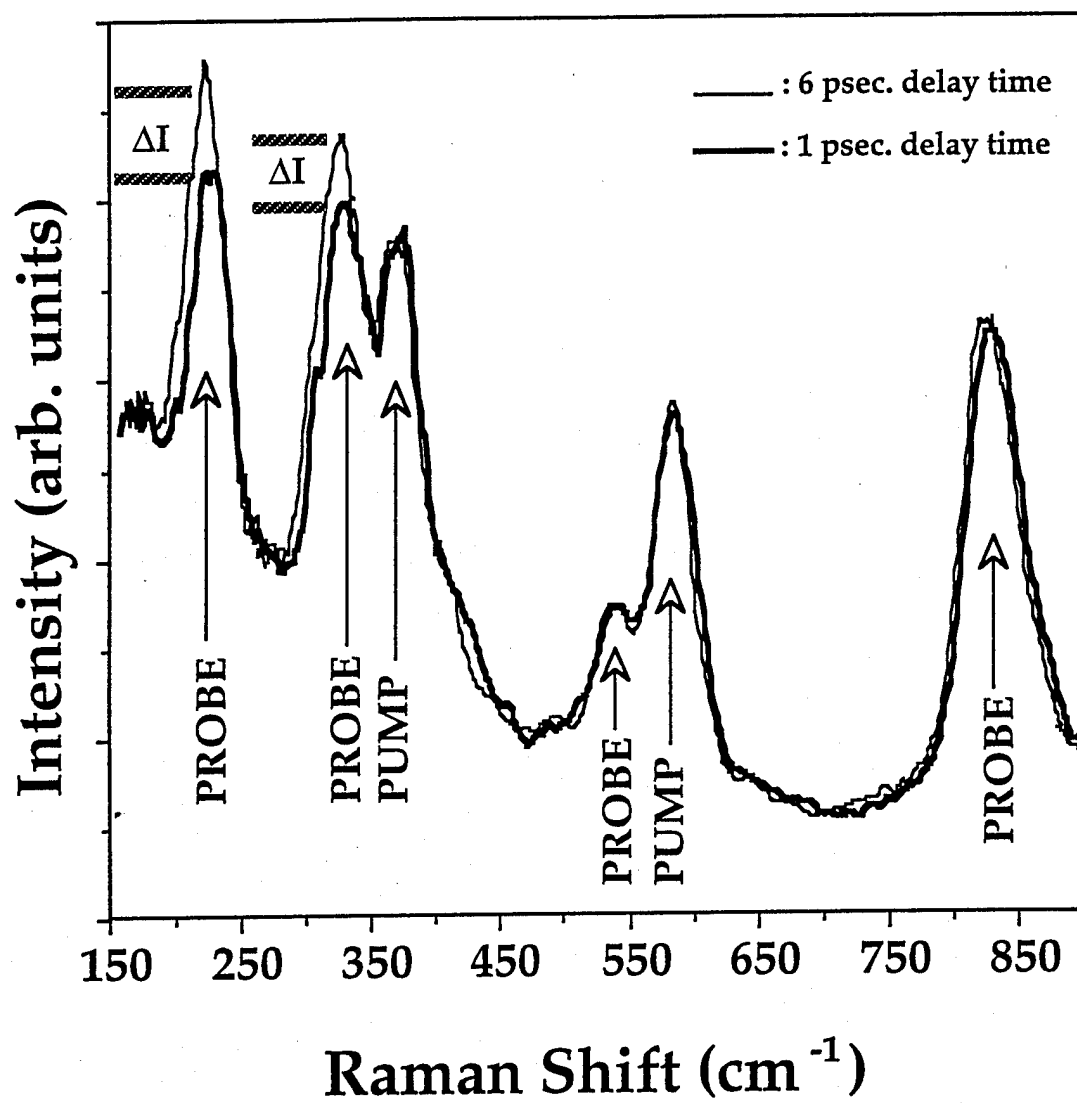


Figure 1

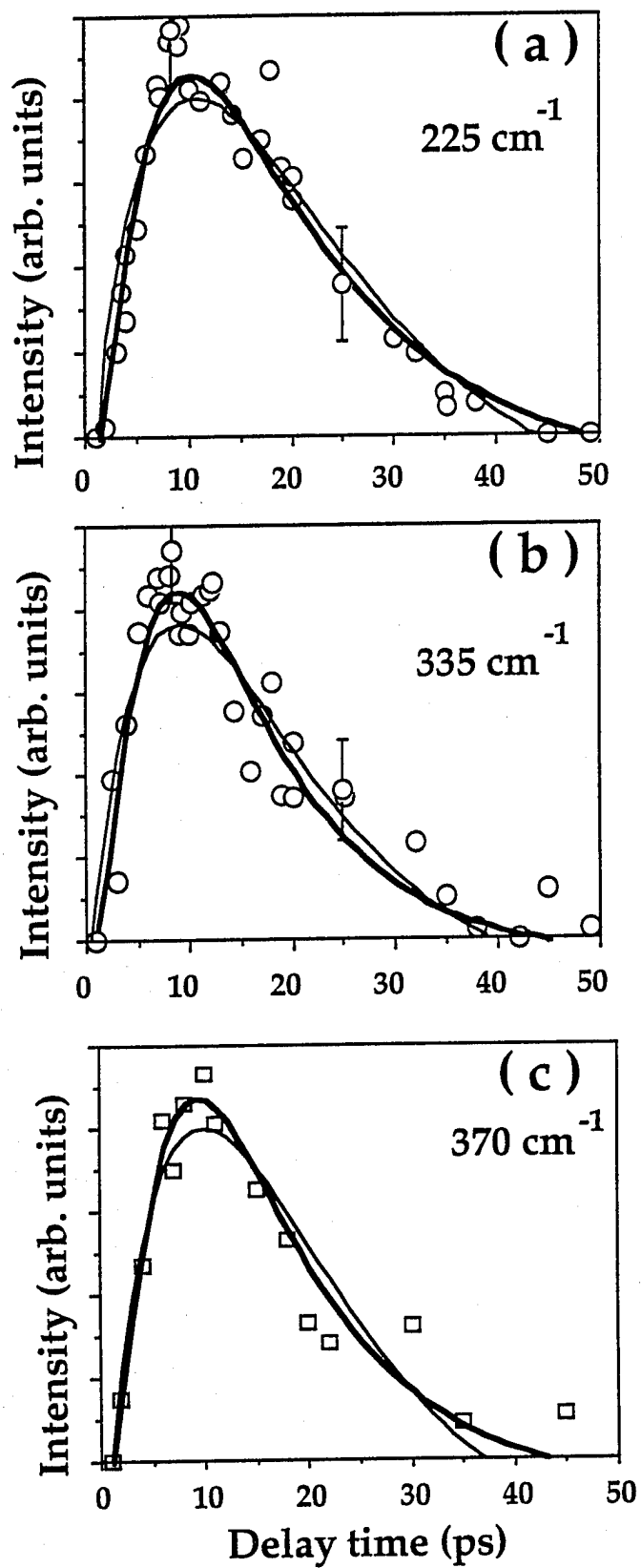


Figure 2

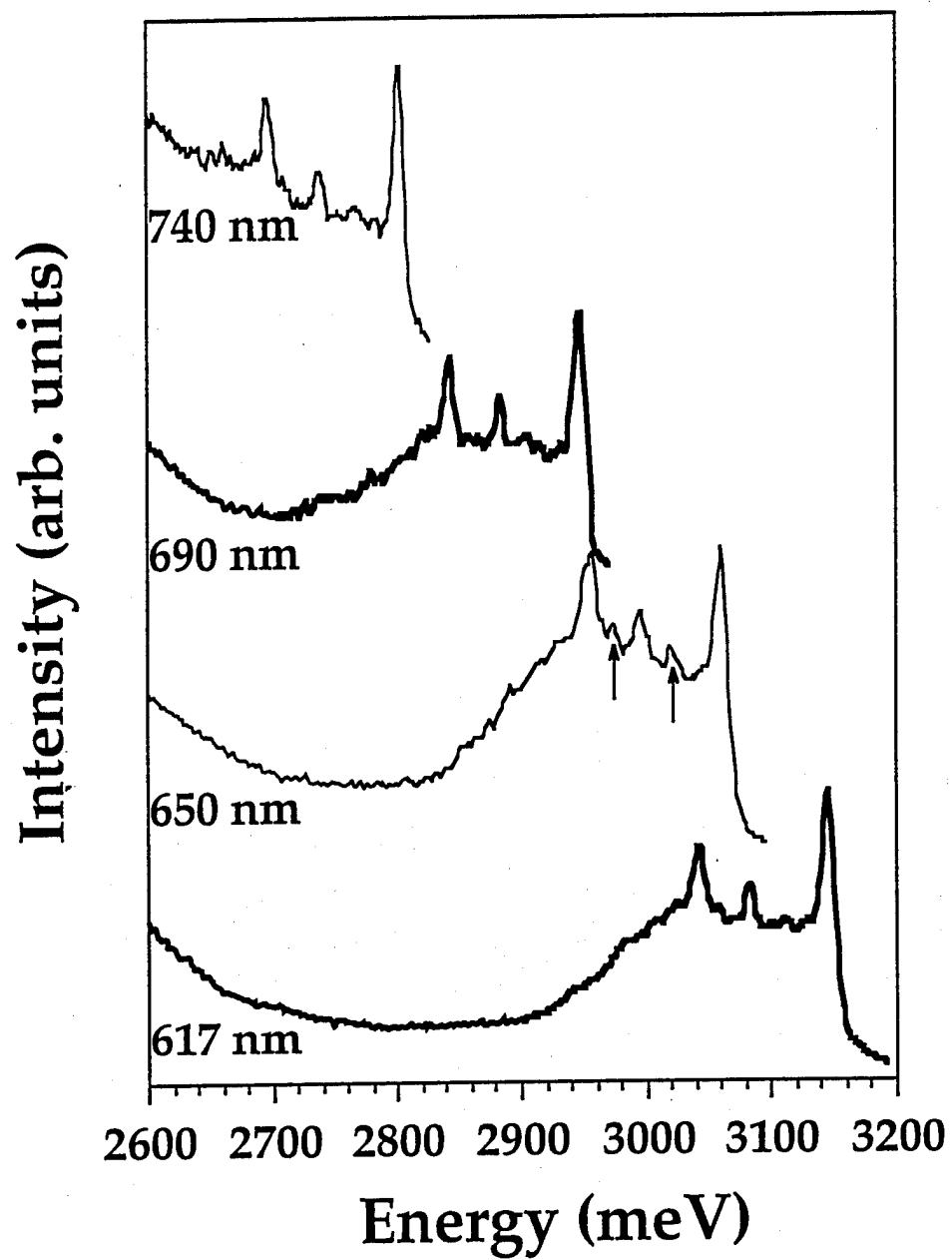


Figure 3

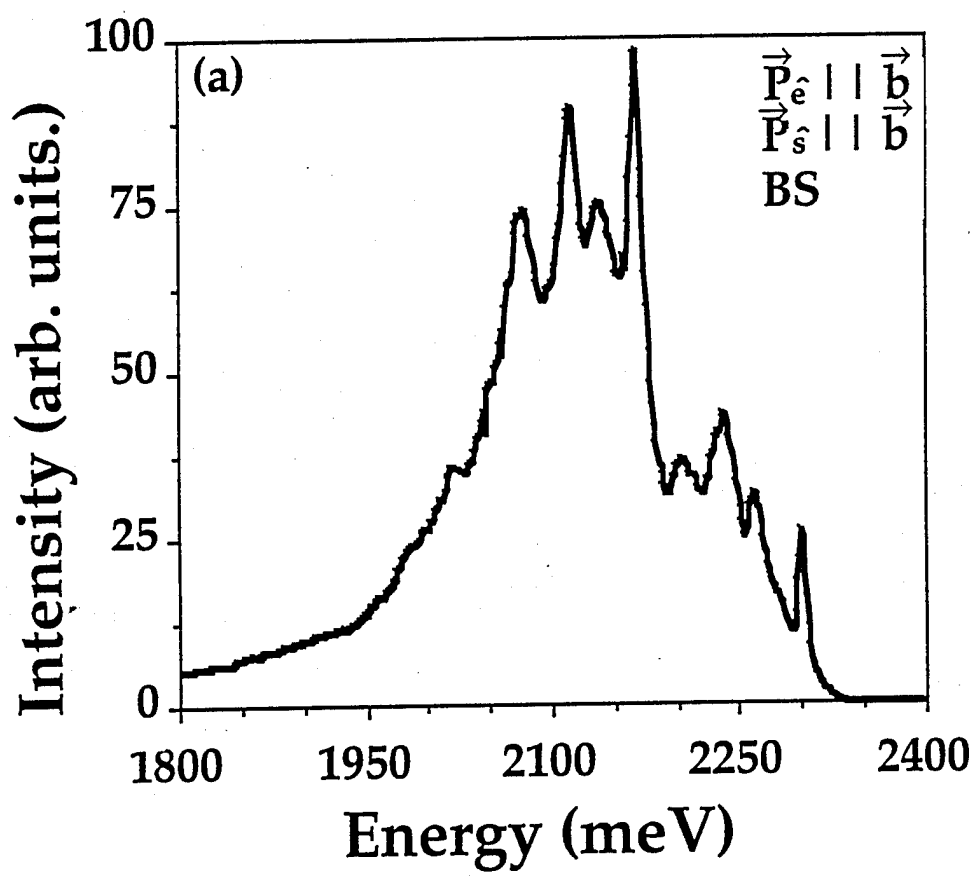


Figure 4

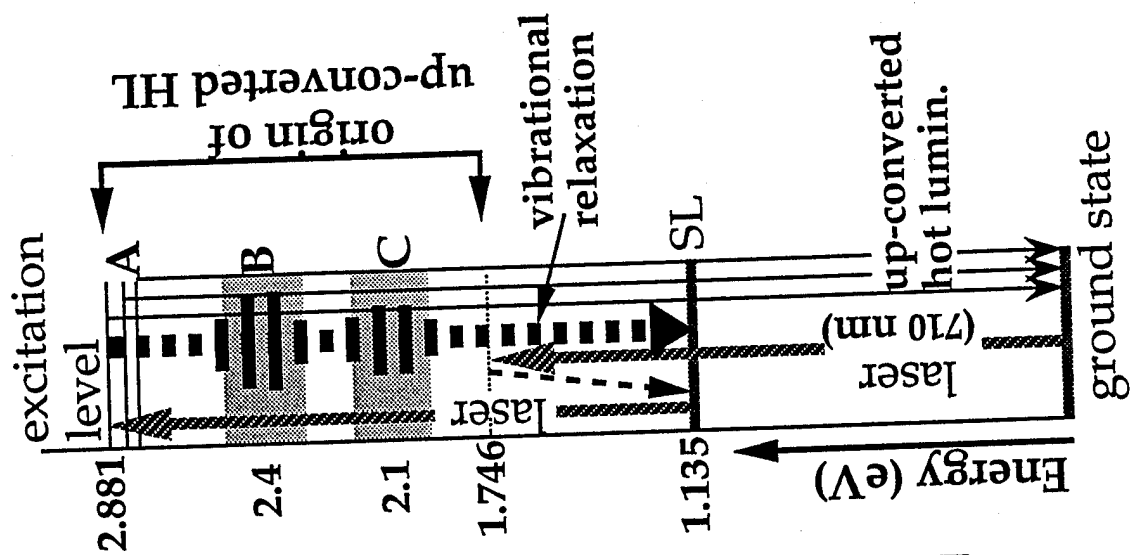
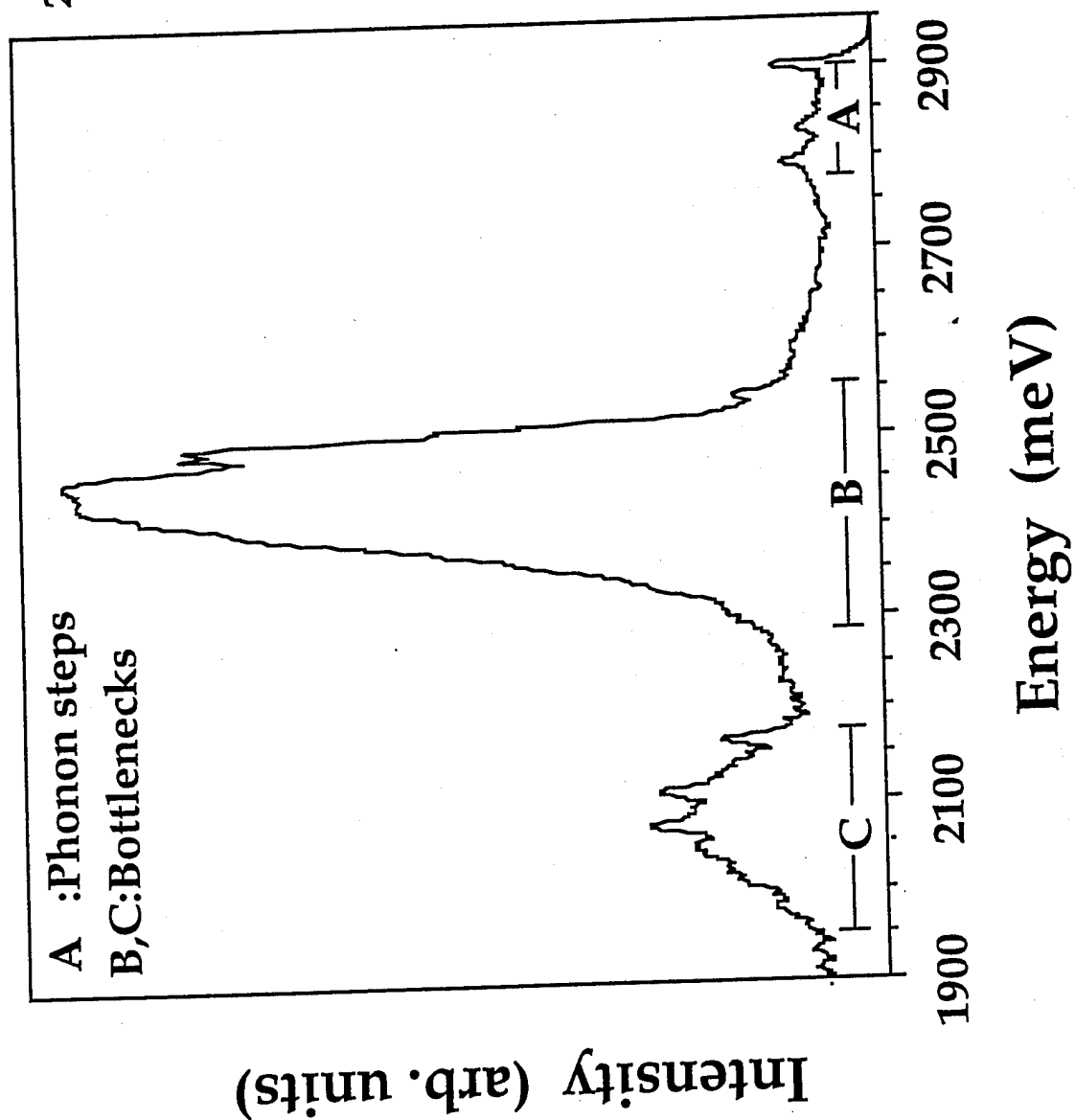


Figure 5

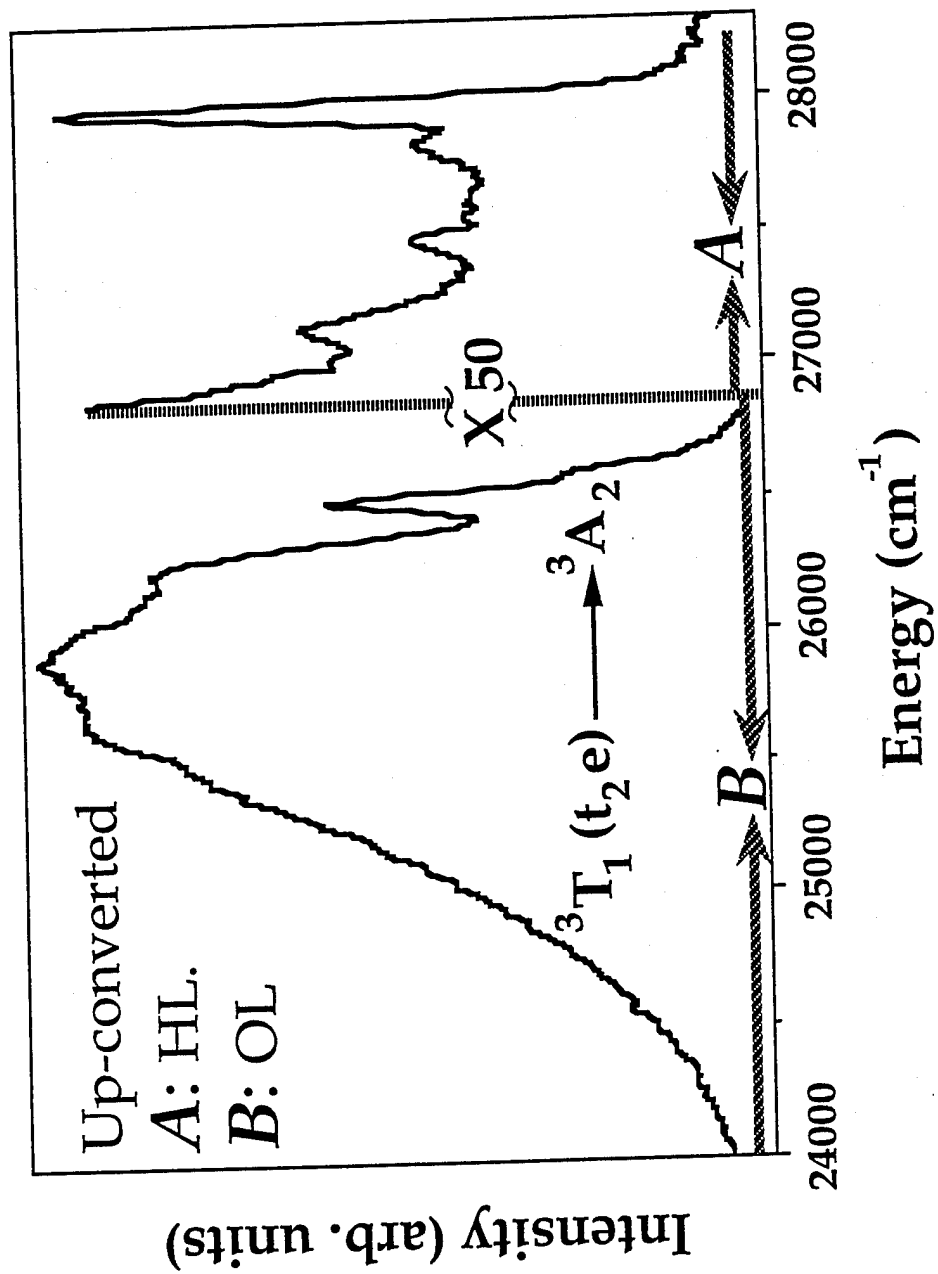


Figure 6



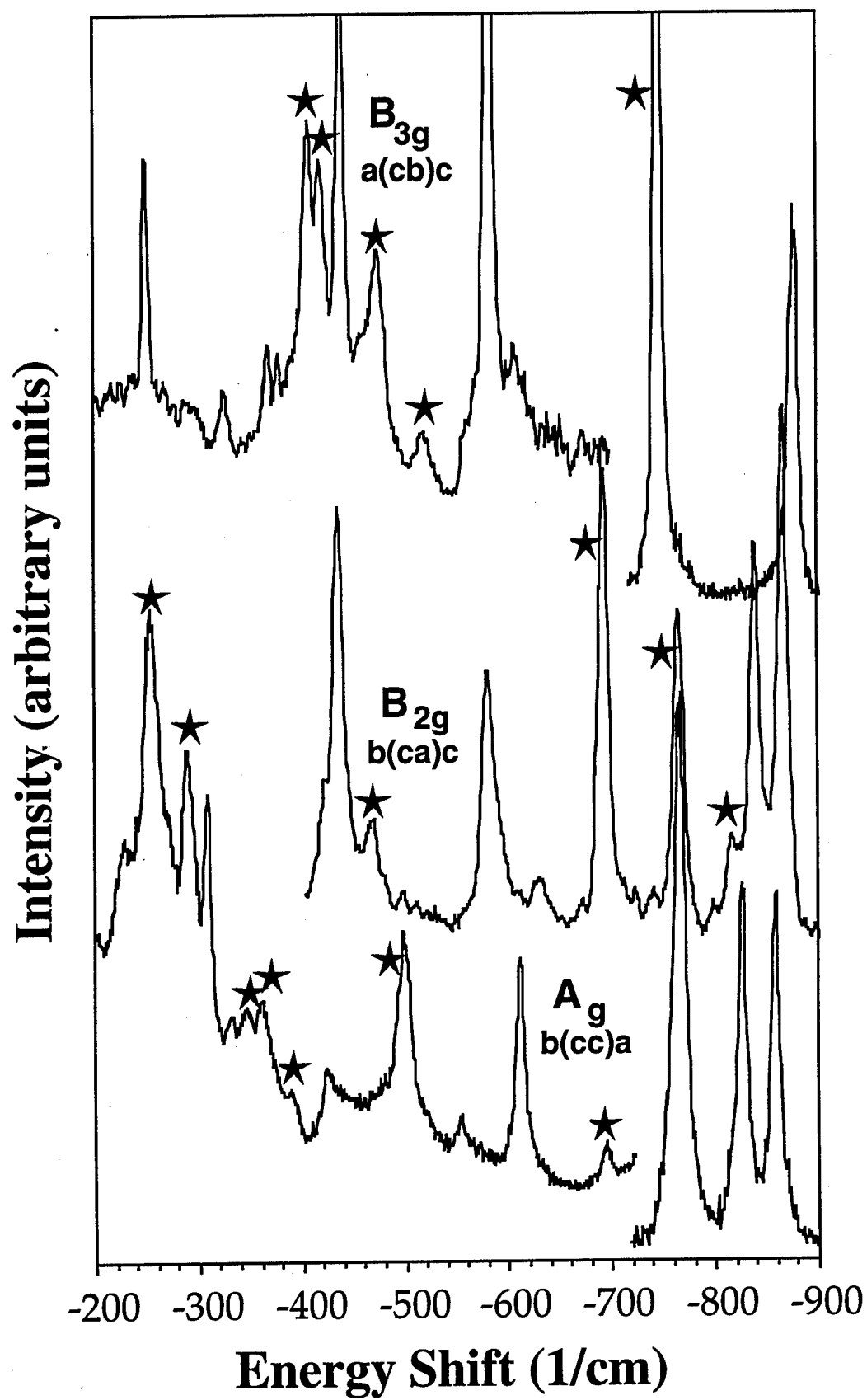
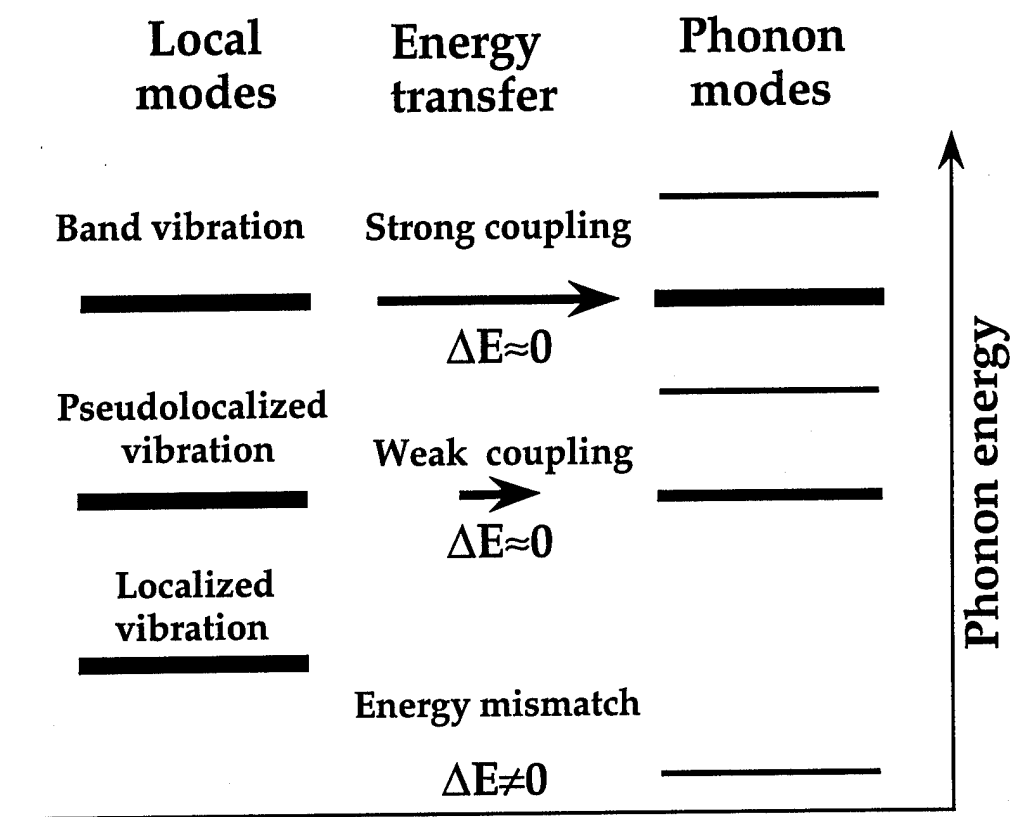


Figure 7



**Figure8**

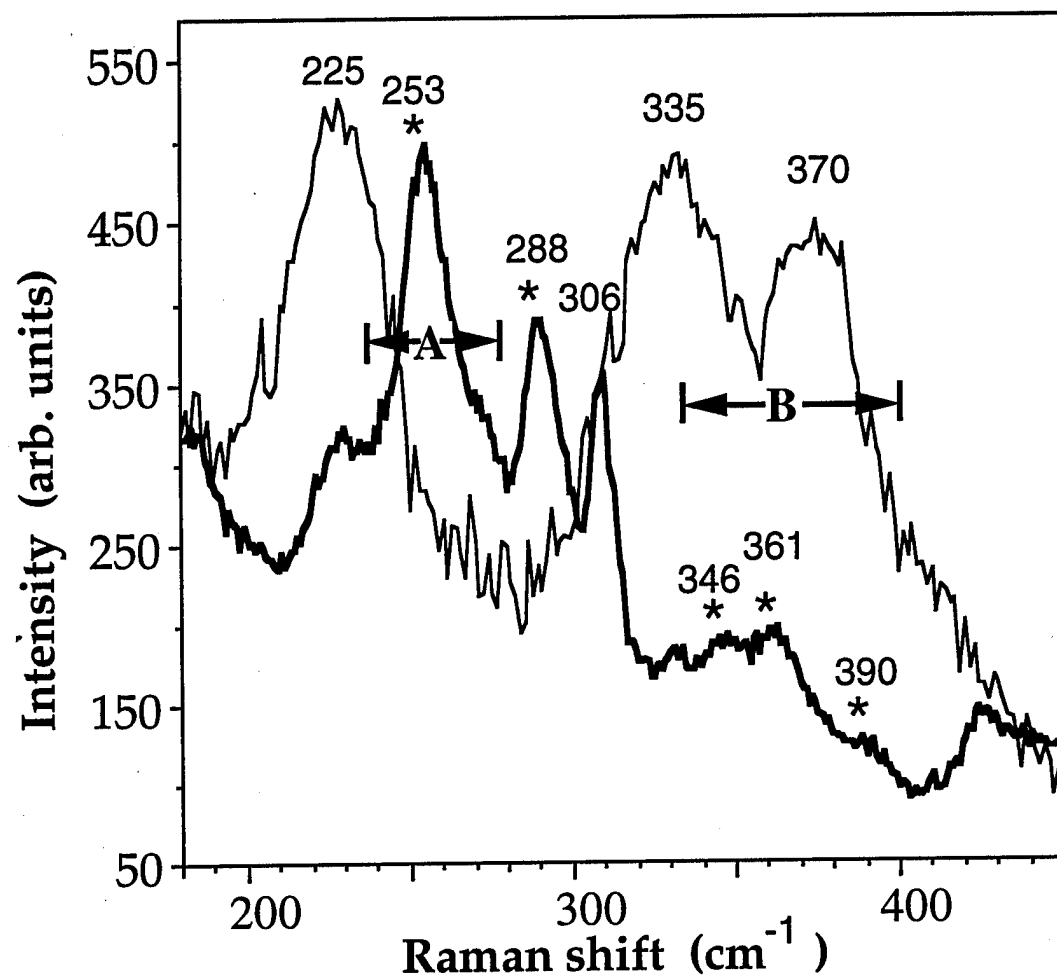


Figure 9

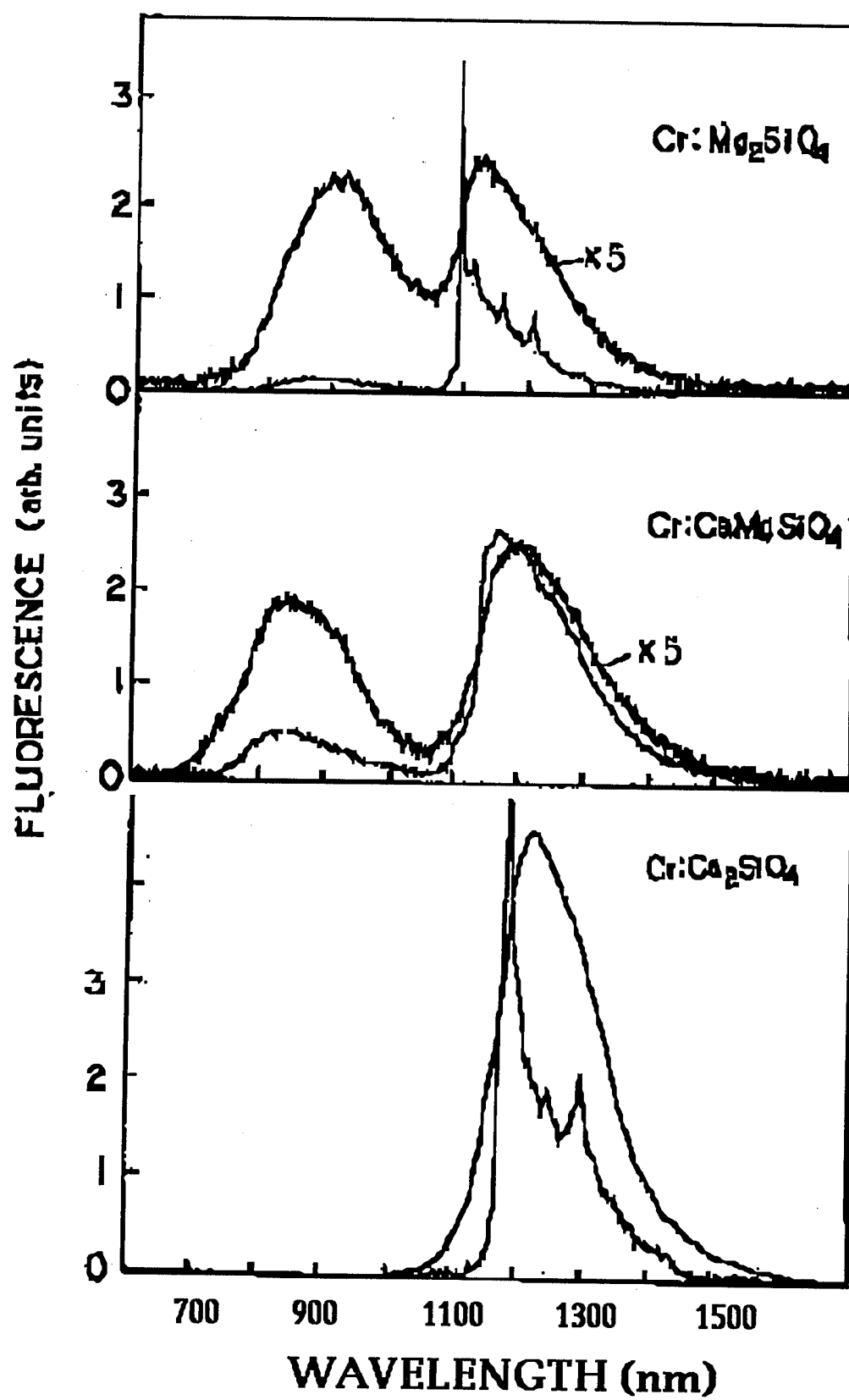


Figure 10

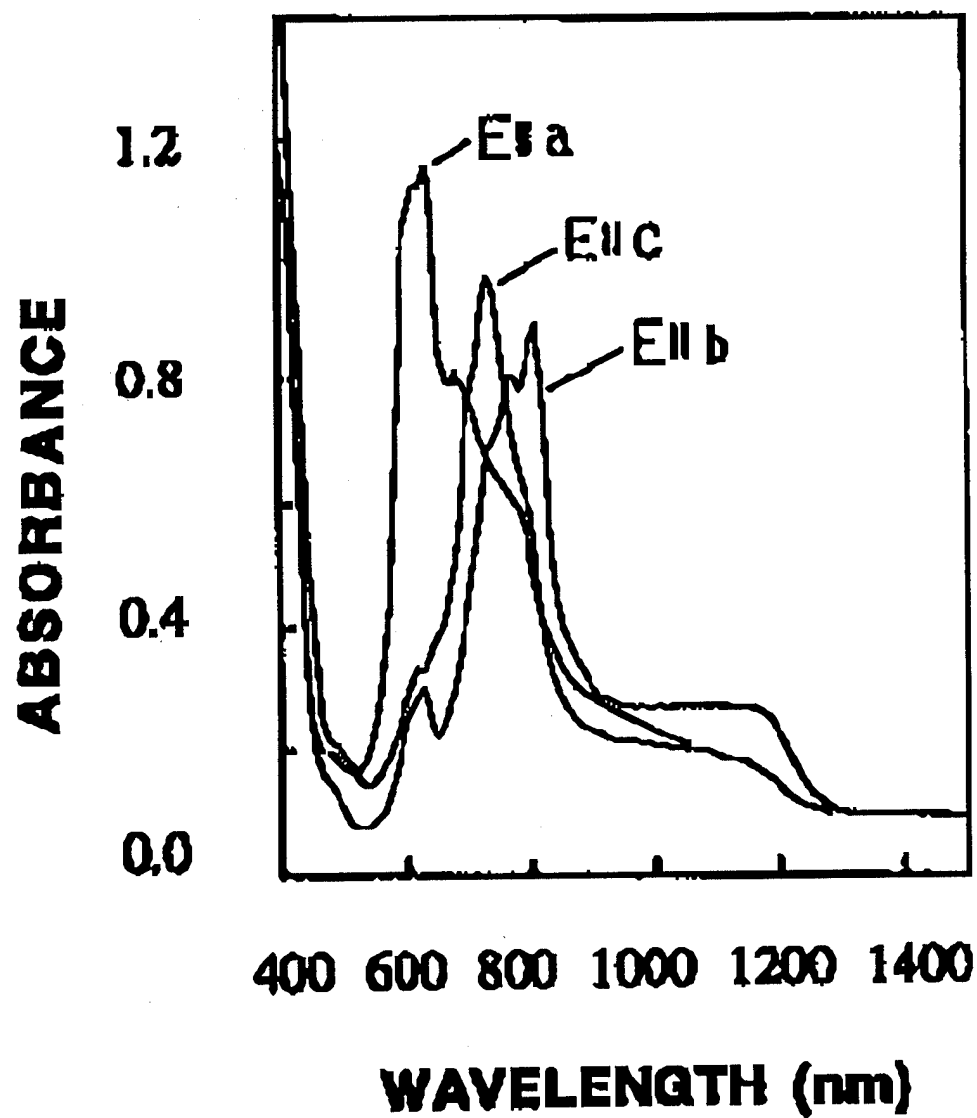


Figure 11

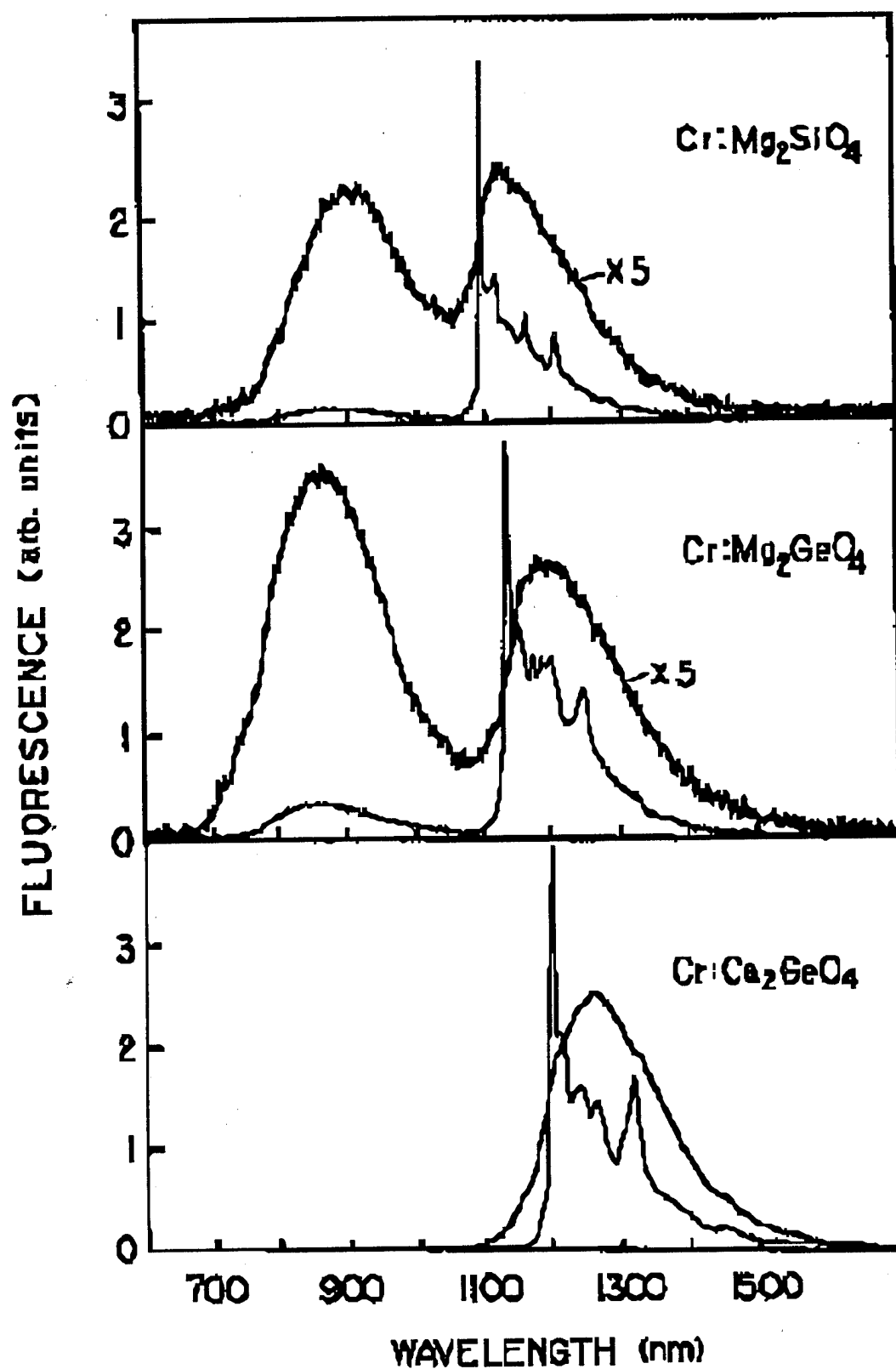


Figure 12